Carbon 242 (2025) 120416

Contents lists available at ScienceDirect

Carbon

journal homepage: www.elsevier.com/locate/carbon

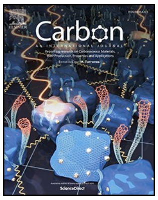

Mechanical strength enhancement of C/SiC–Nb brazed joints through ultrafast high-temperature non-equilibrium surface high-entropy metallization

Peixin Li [a,1], Zeyu Wang [b,1], Yicheng Chen [c], Hassaan Ahmad Butt [d], Zilong Zhang [a], Ziyao Huang [a], Tianlei Zhang [a,e], Liang Qiao [f], Ying Zhong [c], Dmitry Krasnikov [d], Albert Nasibulin [d], Jian Cao [a], Yaotian Yan [a,*], Junlei Qi [a,**]

[a] *State Key Laboratory of Precision Welding & Joining of Materials and Structures, Harbin Institute of Technology, Harbin, 150001, China*
[b] *School of Material Science and Engineering, Jiangsu University, Zhenjiang, 212013, China*
[c] *Sauvage Laboratory for Smart Materials, School of Integrated Circuit, Harbin Institute of Technology (Shenzhen), Shenzhen, 518055, China*
[d] *Skolkovo Institute of Science and Technology, Nobel Street 3, Moscow, Russian Federation*
[e] *Beijing Institute of Remote Sensing Equipment, Beijing, 100854, China*
[f] *Key Laboratory of Materials Design and Quantum Simulation, College of Science, Changchun University, Changchun, 130022, China*

ARTICLE INFO

Keywords:
C/SiC
Brazed joints
High-entropy metallized layer
Ultrafast high-temperature non-equilibrium temperature field
Residual stress

ABSTRACT

To address the challenges of high residual stress and limited high-temperature performance in C/SiC composites brazed with Nb joints using AgCuTi filler alloy, we propose a novel method of high-entropy surface metallization within an ultrafast, high-temperature, non-equilibrium temperature field (UHNF). This approach utilizes rapid heating and quenching induced by the Joule effect to produce a superior quality high-entropy metallized layer (HEML) on the C/SiC surface. Experimental results demonstrate that the brazed joints, including a 170 μm HEML, exhibit improved mechanical properties at both room temperature and 500 °C, overcoming key challenges associated with traditional joining methods. The method effectively mitigates residual stress, enhances resistance to plastic deformation, and improves the high-temperature performance of the AgCuTi filler alloy. By reducing the formation of brittle reaction layers and improving stress dissipation, this technique significantly boosts the mechanical robustness and thermal stability of brazed joints. The use of high-entropy alloys (HEAs) stabilizes the interface and extends the operational temperature range of the AgCuTi alloy. This innovative approach offers a promising strategy for overcoming the performance limitations of aerospace materials, particularly in applications involving large, performance dependent C/SiC–Nb joints.

1. Introduction

The advancement of modern aerospace technology demands materials that are lightweight, display high-strength, and are capable of withstanding elevated temperatures [1–4]. Carbon fiber-reinforced silicon carbide composites (C/SiC) exhibit low density, high strength [5,6], and excellent thermal stability [7,8], making them ideal for aerospace applications [9] including engine combustion chambers and thermal protection systems [10]. In comparison to SiC ceramics, C/SiC offers superior fracture toughness, but due to the inherent difficulty in machining C/SiC, it must be joined with refractory metals to fulfill practical requirements [11].

Niobium (Nb), with its high melting point, ablation resistance, and excellent plasticity, is often selected to join C/SiC for aerospace applications [12,13]. This combination, however, presents significant technical challenges. This is noticed particularly for large brazed joints such as next-generation nozzle structures with diameters exceeding 110 mm, which must endure ultra-high speeds and thrust forces. Such performance requirements intensify processing difficulties since a strong control on interfacial structure and stress relief is needed. Notably, to

---

* Corresponding author.
** Corresponding author.
E-mail addresses: ytyanhit@hit.edu.cn (Y. Yan), jlqi@hit.edu.cn (J. Qi).
[1] These authors contributed equally.

https://doi.org/10.1016/j.carbon.2025.120416
Received 13 February 2025; Received in revised form 12 April 2025; Accepted 9 May 2025

maintain operational integrity at 500 °C, the joints must retain strengths above 40 MPa. Achieving reliable C/SiC–Nb joining is thus critical to overcoming current aerospace engineering limitations [14].

Presently, flange-based mechanical joining is commonly used for C/SiC and Nb joints. Although mechanically robust, they are heavy, complex, and offer limited airtightness, hindering lightweight designs necessary for aerospace applications [12]. In contrast, active brazing can simplify joint structure, reduce weight, and enhance airtightness [15]. AgCuTi filler alloy [16,17] is widely utilized in high-temperature brazing for its suitable melting point, mechanical strength, thermal conductivity and provision of other advantages for C/SiC–Nb joining. However, active brazing presents inherent challenges: (1) Significant differences in thermal expansion coefficients (CTE) between C/SiC and Nb generate high residual stress at the joint, directly compromising the structural integrity of the brazed joints [18–20]; (2) The formation of a continuous brittle reaction layer on the C/SiC surface increases susceptibility to brittle fracture due to stress concentration [21,22]; (3) AgCuTi alloy rapidly softens above 500 °C due to the presence of solid solution Ag (s, s), restricting its maximum operating temperature [23]. Conventional methods, such as particle reinforcement and interlayers aim to mitigate residual stress, but their performance enhancement is limited by issues like brittleness at the C/SiC interface and uneven reinforcement distribution [24,25].

Surface metallization has emerged as an alternative method to alleviate residual stress in brazed joints [26]. Compared with particle reinforcement or interlayer application, surface metallization can reduce thermal mismatches, lower residual stress, and improve wettability at the interface, preventing the formation of brittle reaction layers. Nevertheless, conventional metals used in metallization react with composite surfaces, resulting in brittle layers that limit joint mechanical load bearing capacity and performance. High-entropy alloys (HEAs) introduce a new approach, characterized by multiple principal elements (typically more than four) with concentrations between 5 and 35 atomic percent [27]. The configurational entropy of HEAs stabilizes the solid solution, inhibiting brittle reaction layers at the interface [28]. In addition, their lattice distortion effect [29] enhances toughness, allowing stress dissipation and reduced stress concentrations in the joints [30].

Recent advancements [31] in ultrafast, high-temperature, non-equilibrium temperature field (UHNF) technology offer potential for metallizing C/SiC surfaces without exacerbating residual stress. The ultrafast high-temperature non-equilibrium temperature field (UHNF) is a novel processing technique that leverages Joule heating to achieve rapid heating (up to 3000 K) and quenching rates exceeding 10^3 K/s. This method minimizes thermal accumulation and suppresses atomic diffusion, enabling the stabilization of high-temperature phases at room temperature. UHNF has been widely applied in advanced material synthesis due to its ability to create non-equilibrium microstructures with enhanced mechanical properties. Through the Joule heating effect [20], UHNF can achieve rapid heating to temperatures as high as 3000 K, and when followed by swift quenching, can effectively limit heat accumulation and stress. UHNF minimizes reaction between HEAs and composites, suppressing brittle interfacial compound formation and facilitating lattice distortion within HEA. This sequential phenomenon can enhance the AgCuTi alloy high-temperature range, while ensuring reliable C/SiC–Nb joining.

This study proposes a UHNF-induced high-entropy metallization approach for the surface of C/SiC composites to target residual stress and high-temperature performance challenges in large C/SiC–Nb nozzles. By leveraging HEA properties and UHNF's rapid heating and quenching characteristics, the approach aims to mitigate brittle compound formation, enhance stress relief, and extend the high-temperature applicability of AgCuTi filler alloy in brazed joints.

2. Computational and experimental methods

2.1. Experimental method

The C/SiC sheets were first sectioned into 5 × 5 × 5 mm^3 blocks, and then immersed in ethanol to remove any surface contaminants. A high-entropy alloy (HEA) powder (FeCoCrNiMo) was mixed with N-methyl-2-pyrrolidone (NMP) solution of polyvinylidene fluoride (PVDF) in a concentration of 0.1 g/L and stirred until the suspension thickened. The vertical surface of the carbon fiber growth direction was selected as the metallization surface onto which the HEA mixture was uniformly applied. The specimen assembly was then placed on the ultrafast high-temperature non-equilibrium temperature field (UHNF) platform. Carbon fabric was wrapped around both sides of the specimen, and each side was connected to a power source before being shielded in an argon atmosphere. The power source voltage was set to 31 V, and the temperature was monitored using an infrared thermometer. Metallization currents ranged from 45 to 55 A, and process durations varied between 10 and 20 s.

Nb sheets were cut into 10 × 10 × 5 mm^3 blocks using electric spark cutting, then being soaked in ethanol for surface degreasing. The convex Nb surfaces were polished with sandpaper and ultrasonically cleaned for 10 min. This resulted in smooth, flat blocks. A 500 μm-thick AgCuTi filler alloy foil was also prepared by polishing off surface oxides and performing a 10-min ultrasonic cleaning in ehtanol. The joints were assembled as C/SiC/HEA/AgCuTi/Nb and placed in a vacuum brazing furnace. The brazing process involved a 10 °C/min heating rate to 150 °C, followed by a 10-min hold to volatilize adhesives. The temperature was subsequently raised to 880 °C at 10 °C/min, with a 10-min hold at a vacuum of 1×10^{-4} Pa, and then cooled to room temperature at a rate of 5 °C/min.

Characterization techniques including scanning electron microscopy (SEM) and electron dispersive spectroscopy (EDS) were employed to analyze the microstructure and elemental composition of the high-entropy metallized layer (HEML) and brazed joints. X-ray diffraction (XRD) was conducted to examine phase composition, while X-ray photoelectron spectroscopy (XPS) was utilized to investigate interfacial reaction layers. Shear strength was evaluated using an AGXplus testing machine at room temperature and 500 °C, with an average calculated across three samples at each condition.

2.2. Computational method

This study employed density functional theory (DFT) calculations using the CASTEP program for first-principle quantum mechanical simulations. The Perdew-Burke-Ernzerhof (PBE) exchange-correlation functional within the generalized gradient approximation (GGA) was applied. Self-consistent field (SCF) calculations solved the Kohn-Sham equation with an SCF energy convergence threshold of 5.0×10^{-6} eV/atom. Structural optimization followed the BFGS method with tolerances set at $<1.0 \times 10^{-5}$ eV/atom for system energy errors, <0.05 GPa for stress deviation, <0.3 eV nm^{-1} for atomic force, and $<10^{-4}$ nm for displacement. DFT calculations used a 4 × 4 × 1 k-point grid and 500 eV cutoff energy. Ultrasoft pseudopotentials and a 0.05 $Å^{-1}$ Monkhorst-Pack grid ensured convergence. In this work, the HEA correlation model selected the optimal crystal orientations of phase in XRD, including SiC (0 0 1), carbon (0 0 1), FCC (1 1 1), BCC (1 1 0), μ-phase (1 1 0) and σ-phase (1 1 0). Ti elements appear as small liquid molecules in the brazing process. All the models finally converge after structural optimization.

The calculation formula of adsorption energy is shown in Eq. (1):

$$W_{ad} = \left(E_{ad}^{A} + E_{ad}^{B}\right) - E_{ad}^{A/B} \tag{1}$$

where W_{ad} is the adsorption energy of the model. where $E_{ad}^{A/B}$ represents the total energy of the interface model, E_{ad}^{A} and E_{ad}^{B} denote the energies of individual slab models.

Abaqus software was used for finite element modeling to analyze residual stress distribution within the brazed joints.

3. Results and discussion

Using UHNF, a high-entropy metallized layer (HEML) was successfully formed on the C/SiC surface. As illustrated in Fig. 1a, the HEML adhered uniformly to the C/SiC surface, with both sides of the joint wrapped in carbon fiber to facilitate rapid Joule heating. This created the UHNF. The ultrafast heating and subsequent rapid quenching resulted in enhanced lattice distortion within the HEAs, significantly improving the stress-bearing capacity of the HEML. Conducted in an argon-protected atmosphere, this process minimized oxidation, ensuring the formation of a high-quality metallized layer. Fig. 1b illustrates the temperature profiles of the UHNF process under varying current and duration settings. The observed temperatures rose and stabilized within a narrow fluctuation range, which is essential to achieve uniform HEML properties across the specimen. For instance, as the current was increased from 45 A, 50 A–55 A, the corresponding temperatures

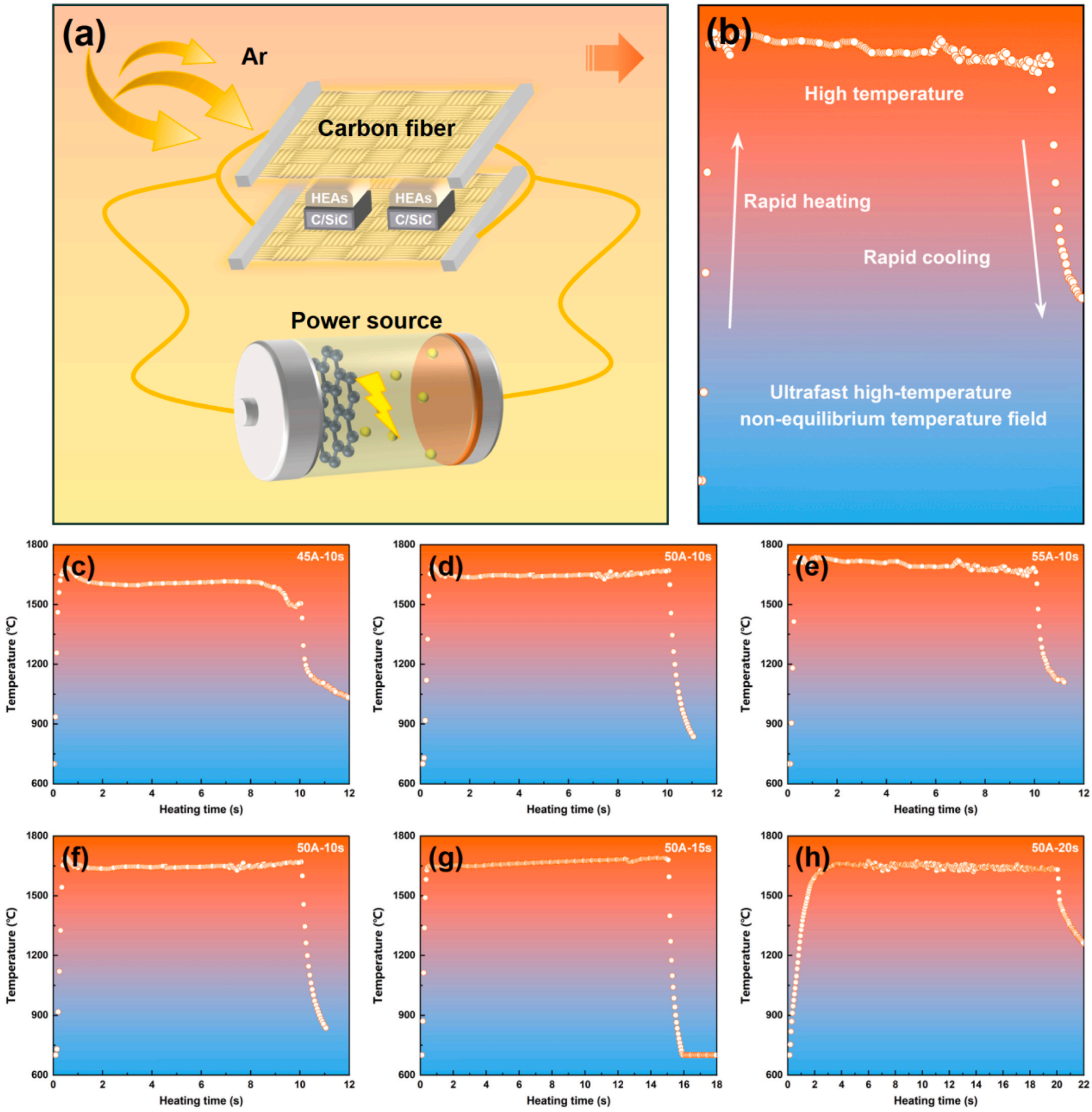

Fig. 1. Diagram of the UHNF process and temperature field

(a) High-entropy surface metallization of C/SiC in UHNF, (b) The temperature profiles of the process under varying current and durations, (*c*–e) 45 A, 50 A, 55 A current under 10 s, and (f–h) 10 s, 15 s, 20 s of heating under 50 A. (A colour version of this figure can be viewed online.)

reached approximately 1600 °C, 1650 °C, and 1700 °C, demonstrating that higher currents result in proportionally higher temperatures. The rapid cooling process of UHNF enables rapid hardening of the HEML. Moreover, the temperature stability across different durations (10 s, 15 s, and 20 s) suggests that UHNF maintains process stability over extended times, which is critical for achieving repeatable and homogeneous metallization.

In Fig. 2, each subfigure (**a-d**) highlights how the current and time influence HEML thickness and uniformity. Observing each individually reveals their interaction and elucidates on how to achieve an optimal configuration that balances thickness, integrity, and defect minimization. Fig. 2a shows HEML thickness decreasing with increasing current (45 A, 50 A, 55 A) and time (10 s, 15 s, 20 s). This is due to enhanced fluidity and atom motion at higher currents and longer exposure, which cause splashing and thinning of the HEML during rapid cooling. For example, at 45A for 10 s, the thickness is about 350 μm, but it decreases to around 170 μm at 50 A for 10 s, illustrating that the layer is sensitive to thermal input. This can further be used for identifying an optimal range for structural support with minimal defects. In Fig. 2b, the typical interfacial structure of the 350 μm HEML at 45 A for 10 s shows continuity with visible porosity. This porosity, likely due to insufficient heat, can create stress concentration points, reducing the effectiveness of the layer in dissipating residual stress. Incomplete phase fusion also suggests that lower current and shorter time do not fully optimize phase distribution, potentially weakening the joint's integrity. Fig. 2c shows a 170 μm HEML formed at 50 A for 10 s, appearing to be optimal with a uniform, defect-free surface. This thickness provides sufficient material for stress distribution and structural continuity, minimizing defects. The 50 A-10 s setting achieves an ideal thermal environment, allowing cohesive layer formation without excess atom mobility or splashing, enhancing stress-relieving capacity. In Fig. 2d, a ~50 μm HEML formed at 55 A for 10 s or 50 A for 15 s is seen to have reduced thickness and some irregularities. The higher current or longer time increases atomic mobility, causing splashing that thins the layer and reduces stability. While relatively flat, this thinner layer is less effective at stress relief and may not evenly distribute thermal stresses, impacting joint performance in high-stress conditions. This suggests that while increasing current or time can add thermal input, it risks destabilizing the HEML with excessive thinning and internal weaknesses.

The surface structure features of 350 μm, 170 μm and 50 μm HEMLs are shown in Fig. 3a–c. It can be seen that the structure decreases with the decrease of thickness, and the surface becomes gradually smooth, which is consistent with the structure features shown in Fig. 2. The microstructure of the HEML was analyzed following the rapid heating and quenching induced by the UHNF process. A representative region of the 170 μm HEML was selected for detailed phase analysis, with the results shown in Fig. 3d–j. Fig. 3d–i illustrate the elemental distributions across the HEML, while Fig. 3j presents the X-ray diffraction (XRD) analysis. The analysis reveals that Fe and Co are predominantly concentrated within localized, leaf-like structures, while Cr is dispersed across several bulk phases, with one particular bulk phase showing a higher concentration. Ni is distributed across all phases except the leaf phase, exhibiting aggregation in specific regions. Due to its larger atomic radius, Mo stabilizes particular crystal structures and is primarily concentrated within specific bulk phases. Local Fe/Co enrichment formed BCC phases, which improved ductility. While segregation could induce microstress, the HEA's multi-phase structure dispersed stress concentrations, preventing crack initiation. The XRD analysis confirms

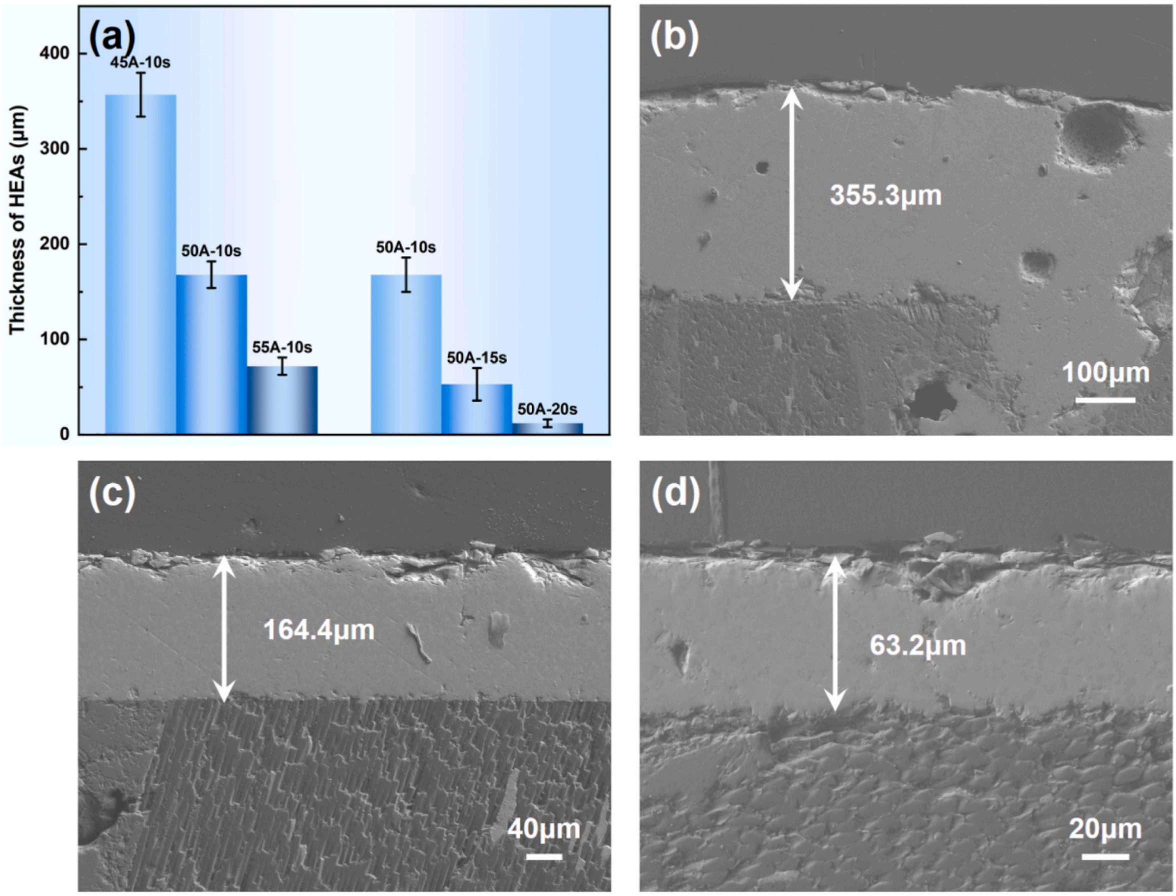

Fig. 2. The thickness of HEML under different experimental conditions
(a) thickness dependency on current and time, and typical interfacial structure of (b) 350 μm, (c) 170 μm, and (d) 50 μm HEMLs. (A colour version of this figure can be viewed online.)

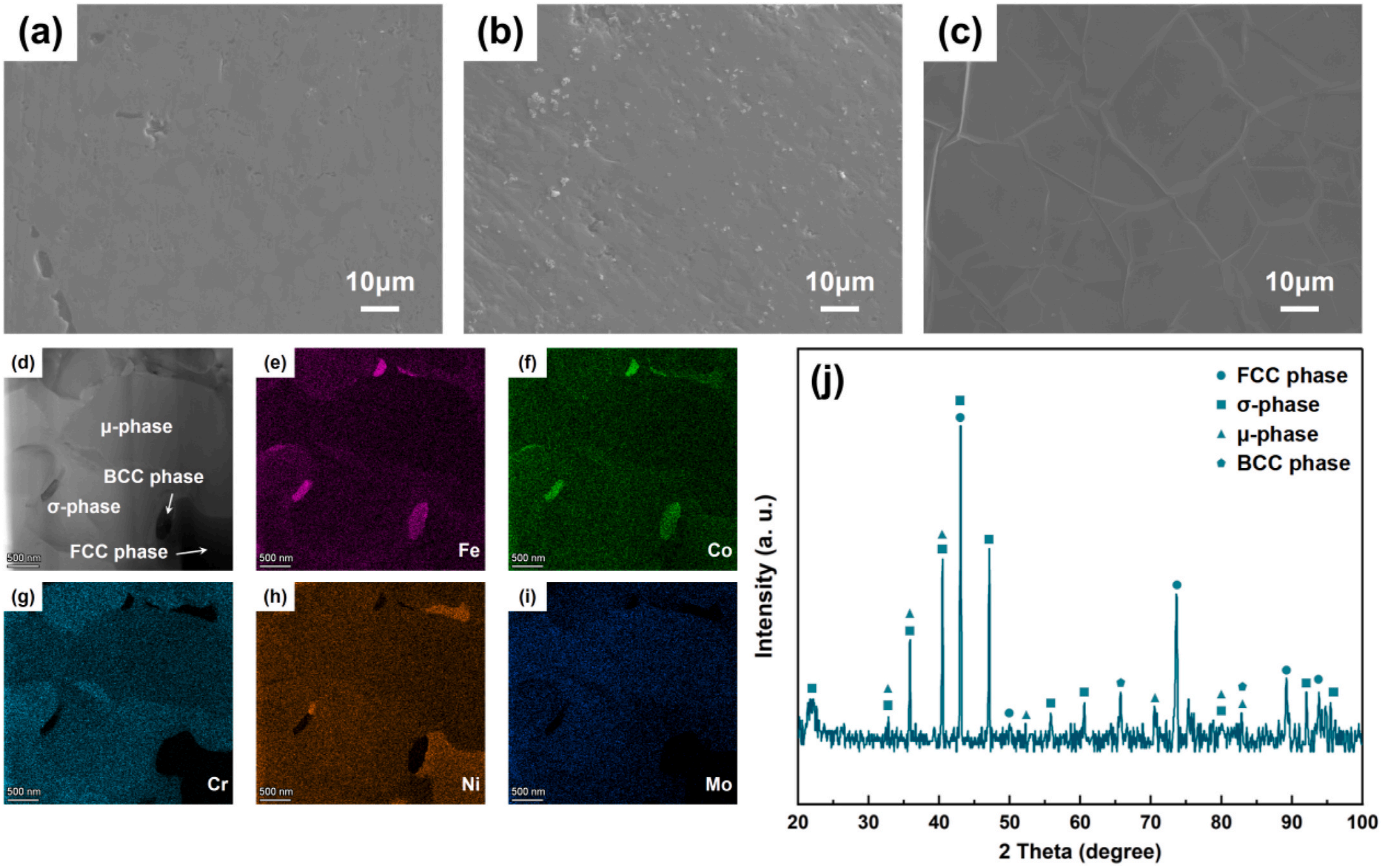

Fig. 3. Microstructure elemental distribution and XRD analysis of HEML after UHNF heat treatment
(a) surface microstructure of 350 μm, (b) 170 μm, and (c) 50 μm HEMLs. (d) phase composition and (e) Fe, (f) Co, (g) Cr, (h) Ni, and (i) Mo elemental distribution of the HEML. j) XRD analysis of the HEML. (A colour version of this figure can be viewed online.)

that the HEML comprises of a combination of FCC, μ, σ, and BCC phases. Research [32,33] indicates that the FCC phase, a common structure in FeCoCrNiMo alloys, is typically enriched with Ni and Co. The region rich in Ni, observed in the lower right corner of the sample, is inferred to be the FCC phase. In addition to the FCC phase, elemental segregation leads to the formation of Cr-enriched σ phase and Mo-enriched μ phase within FeCoCrNiMo. The μ phase is often derived from the σ phase, typically featuring a higher Mo content. The concentration of Cr and Mo further

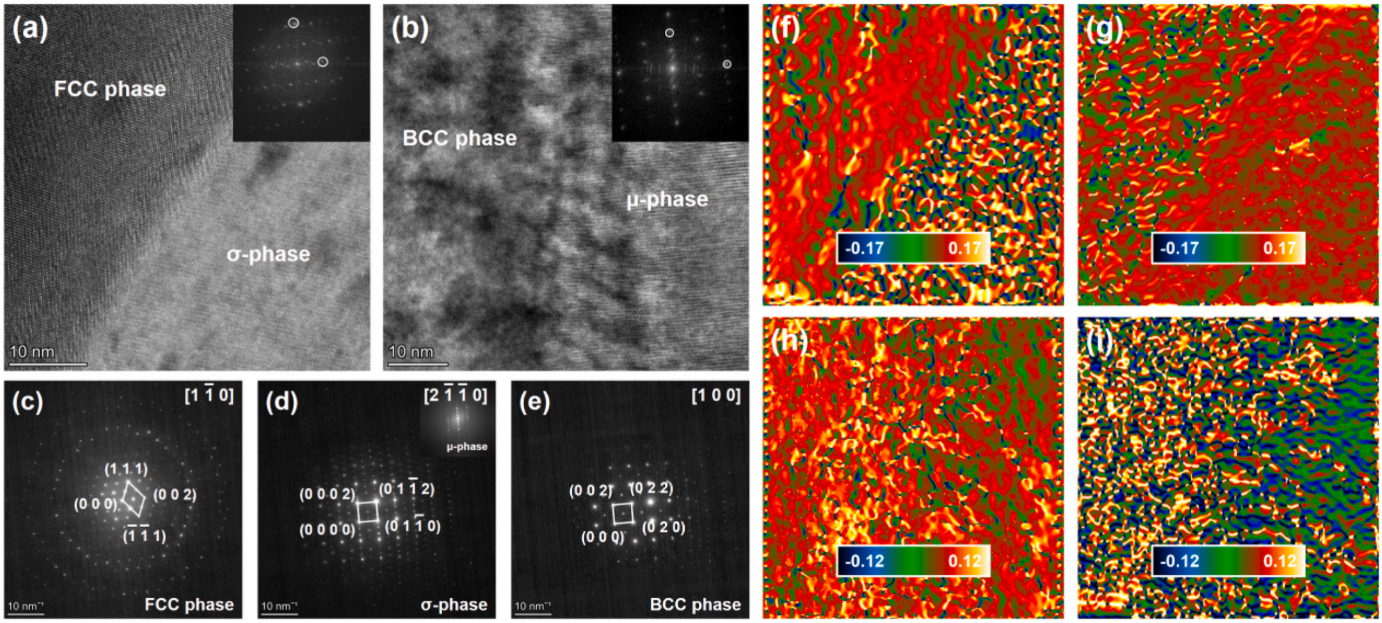

Fig. 4. TEM analysis and geometric phase analysis of HEML microstructure after UHNF. (A colour version of this figure can be viewed online.)

confirms the presence of these phases, with the bulk μ and σ phases displaying a significantly higher content than the FCC phase. The rapid heating of the UHNF reduces the time for atomic diffusion and rearrangement, promoting the preferential formation of μ and σ phases. These phases, driven by high thermodynamic stability, are readily formed at elevated temperatures, while the rapid quenching inhibits atomic diffusion, preventing phase transitions typical of slower cooling. Consequently, these high-temperature phases remain stable at room temperature (RT), which is beneficial for stress mitigation in brazed joints. The μ and σ phases are characterized by high hardness and strength, significantly enhancing the mechanical properties of the HEML. Their stability under high temperatures also allows the HEML to retain its mechanical performance in extreme environments, making it suitable for high-load and stress applications. Additionally, the aggregation of Fe and Co often results in the formation of the BCC phase. This BCC structure, attributed to Fe and Co segregation under non-equilibrium conditions, remains stable due to rapid quenching, which prevents the formation of more stable phases. The coexistence of BCC, μ, σ, and FCC phases within the HEML forms a complex polyphase structure, where the synergistic interactions among these phases optimize overall mechanical properties.

Moreover, Fig. 4 reveals the beneficial lattice distortion across phase interfaces within the HEML, highlighting how the UHNF process facilitates stress relief for joint durability. At the FCC-σ phase interface (Fig. 4a), significant strain results from lattice mismatch, promoting dislocation movement and enabling effective stress distribution. This distortion creates pathways for plastic deformation, allowing the HEML to absorb thermal and mechanical stresses more effectively. Similarly, the BCC-μ interface in Fig. 4b exhibits distortion, though to a lesser extent, as a dislocation-rich boundary that further enhances stress dissipation, a crucial property for high-load environments. In the FCC phase diffraction pattern shown in Fig. 4c, a highly ordered crystal structure is evident, with high-order Laue spots on the [1–10] zone axis, contributing to the thermal stability of the phase and preserving stress-absorbing lattice distortions during cooling. Meanwhile, the σ and μ phases in Fig. 4d exhibit topologically close-packed structures that resist plastic deformation, with the σ phase showing a tetragonal structure on the [2 -1 -1 0] axis and the μ phase transforming to rhombohedral due to Mo atoms. These phases thus strengthen the HEML, as their robust structures mitigate stress concentrations, preventing fracture. The BCC phase diffraction pattern in Fig. 4e, where Fe and Co aggregate, reveals a retained BCC structure on the [1 0 0] axis due to rapid quenching, which provides a balanced combination of rigidity and ductility for improved stress distribution. Geometric phase analysis in Fig. 4f and g shows tensile strain along the FCC-σ phase interface, reaching +17 %, which supports localized plastic deformation and reduces stress concentration, crucial for brittle fracture prevention. Additionally, the BCC-μ interface strain analysis in Fig. 4h and i indicates a peak of +12 %, where variations in strain create multiple dislocation paths within the HEML. This network of pathways distributes residual stress effectively and preserves joint integrity, even under high temperatures, aligning with the study's goal of stress mitigation. Thus, Fig. 4 demonstrates that UHNF processing induces advantageous lattice distortions and strain gradients, lowering fracture risks and enhancing reliability for high-performance applications.

Interface of (a) FCC/σ and (b) BCC/μ-phases; diffraction spots of (c) FCC, (d) σ-/μ-, and (e) BCC phases; geometric phase analysis of (f, g) FCC/σ-, and (h, i) phase interfaces.

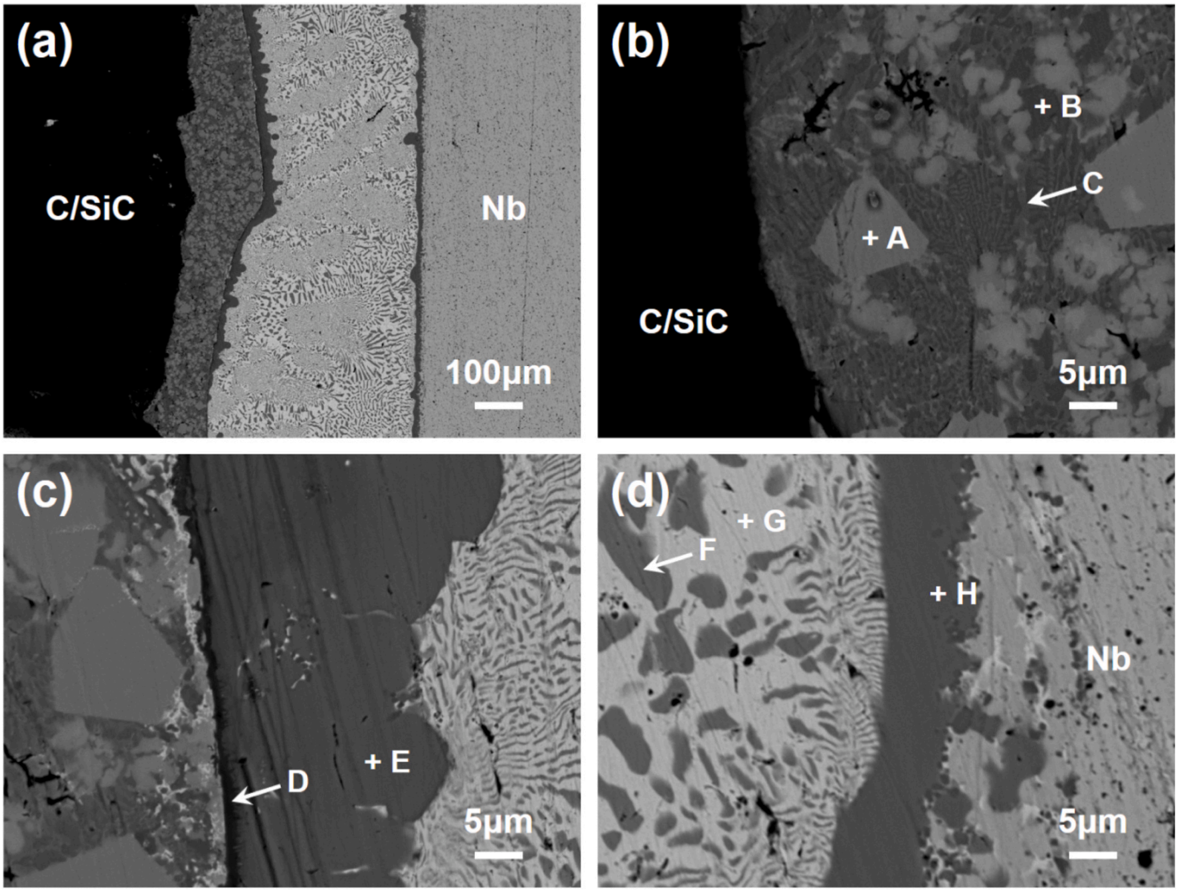

Fig. 5. Typical microstructure of HEML C/SiC and Nb brazed joints
(a) Overall microstructure; interfacial microstructures of (b) C/SiC/HEML, (c) HEML/AgCuTi, and (d) AgCuTi/Nb. (A colour version of this figure can be viewed online.)

To investigate the influence of HEML on C/SiC and Nb brazed joints, Fig. 5 illustrates the microstructural stability and interfacial bonding of the brazed joints, showing how the UHNF-induced HEML effectively enhances joint integrity. The image highlights well-defined phases at both the HEML/C/SiC and AgCuTi/Nb interfaces, where phase continuity minimizes weak points that could lead to fracture. EDS analysis indicates strong phase integrity, with specific elemental distributions contributing to effective bonding and load transfer across the interface. As shown in Table 1, at points A, B, and C in the HEML, high Mo concentration at point A signals the presence of a μ-phase, known for its high hardness and thermal stability. Cr concentration at point B indicates the σ-phase, which adds structural rigidity, while the balanced Fe, Co, and Ni composition at point C suggests an FCC phase that enhances overall ductility. This phase synergy is crucial, as it prevents the formation of brittle compounds and ensures a cohesive bond, particularly under thermal stress. The AgCuTi-HEML interface also demonstrates smooth atomic diffusion, indicating that UHNF metallization minimizes the brittle layers typically found in high-entropy alloys. This atomic diffusion strengthens the interface, reducing residual stresses and stabilizing the bond between the HEML and C/SiC. The high stability observed in Fig. 5 confirms that UHNF-metallized HEML provides both the mechanical robustness and the thermal resistance necessary for reliable high-temperature applications, directly addressing the study's goals of stress mitigation and enhanced joint performance. Notably, Nb exhibited negligible diffusion into the AgCuTi filler or HEML, as evidenced by EDS analyses. This is attributed to the low solubility of Nb in AgCuTi at 880 °C, coupled with the HEML's barrier effect. The HEML's multi-phase structure and lattice distortions impeded Nb migration, while preferential Ti–C/SiC reactions dominated the interfacial chemistry. This limited Nb diffusion preserved the mechanical properties of the Nb substrate, avoiding embrittlement caused by Nb-containing intermetallics.

In the above analysis, the organization of brazed joints was compiled. In addition to the internal organization, the interface was often seen to be the weak region of the brazed joints. The interfaces of C/SiC/HEML and AgCuTi filler alloy/HEML are where further research should be focused. On the basis of the above organizational analysis, we carried out further analysis of these two interfaces. We first analyzed the interface of HEML/C/SiC, which had no obvious interfacial reaction layer. This may be due to its high entropy effect resulting in a thin interfacial reaction layer that is difficult to distinguish. In order to effectively analyze the interface structure of the HEML/C/SiC, as shown in Fig. 6, XPS analysis was performed to determine the joining state. The different valence peaks of each element were fitted according to the XPS data. It can be seen that the five elements of Fe, Co, Cr, Ni and Mo were mainly in the 0-valence state, which is the metal state. In addition, there were 2 and 3 valence atoms in the Fe element, 2 valence atoms in the Co element, 2 and 3 valence atoms in the Cr element, 2 valence atoms in the Ni element and 4 valence atoms in the Mo element. It can be seen that Fe, Co, Cr, Ni and Mo had a certain degree of interfacial reaction with C/SiC. However, the content of these positive valence states was less than that of the 0-valence state, which also proved that the interfacial reaction layer was thin. The interfacial reaction layer generated by the reaction of the elemental state of these materials with C/SiC is often thicker (such as the reaction of Ni and SiC). Therefore, the formation of interfacial brittle compounds can be effectively inhibited by the phase composition of high-entropy state and the UHNF method. The reaction at the interface was divided into the reaction with SiC and the reaction with carbon fiber, which mainly generated carbides and silicides. However, since the reaction alloy was a high-entropy alloy, the products generated at the interface also had high-entropy properties, indicating complex multi-joint interactions and chemical joining. Related studies showed that the reaction of Fe, Co, Ni and SiC only generated silicates, while the reaction of Cr, Mo and SiC produced silicates and carbides at the same time. Although we had established that there was a high-entropy silicide formation at the interface, there was no way to determine the atomic proportion of the high-entropy silicide based on the valence state. For example, Ni presented a bivalent silicide containing NiSi and Ni_2Si [34], and the reaction of Fe, Co, Cr, Ni and Mo with SiC was very complex. Therefore, we used (Fe, Co, Ni, Cr, Mo)Si to represent the silicide produced by the interfacial reaction [35,36]. In addition, Fe, Co, Cr and Mo can react with carbon fibers to form carbides. Ni usually does not form stable carbides with carbon, therefore we used (Fe, Co, Cr, Mo)C to represent the carbides produced by the interfacial reaction. This kind of thin and high-entropy interfacial reaction product can effectively suppress the brittleness of brazed joints caused by thick interfacial reaction layers [2,37,38]. The findings show that the mechanisms present in this work positively contribute to improving the deformation resistance of brazed joints.

We also analyzed the interface between the HEML and the AgCuTi filler alloy, paying particular attention to the role of Ti, given its high chemical reactivity. The elements tendency to accumulate at the interface significantly improves the wettability of the filler alloy, allowing it to spread and fill interfacial gaps more effectively, which is essential for forming a stable bond between the filler and base material. This property makes Ti adsorption a key factor in determining interface stability. Thus, examining the adsorption capacity of various HEML phases relative to Ti atoms provides insights into the robustness of the HEML/AgCuTi interface. Fig. 7a–d depicts the adsorption models for different phases within the HEML, namely FCC, BCC, σ, and μ phases, helping to illustrate how Ti atoms interact with each of these structures. Each phase represents a unique atomic arrangement, which influences how Ti atoms bind to the surface. For instance, the FCC structure has closely packed atoms, creating dense, stable sites for Ti adsorption, which could result in high adsorption energies. Conversely, the BCC structure, with a more open lattice, offers different adsorption dynamics that may lead to slightly weaker bonding interactions. These phase-specific characteristics in the HEML enable it to provide a stable and adaptable bonding environment for Ti atoms. Fig. 7e–f shows the adsorption models for Ti atoms on the C/SiC substrate, providing a comparative view. By analyzing these models, we observe differences in Ti adsorption behavior between the HEML and C/SiC. In the C/SiC structure, the Si and C atoms create adsorption sites that are relatively stable, but exhibit less adaptability compared to the high-entropy alloy. The ability of the HEML to maintain multiple adsorption sites due to its varied phase composition allows it to better anchor Ti atoms, resulting in improved wettability and interfacial bonding strength. To quantify the interaction strength, the adsorption energy of Ti was calculated across 10 selected adsorption sites for each

Table 1
EDS element content table of Fig. 5.

Point	Fe	Co	Cr	Ni	Mo	Si	Ag	Cu	Ti	Nb	Phase
A	6.88	12.81	12.89	21.46	30.70	15.26	–	–	–	–	μ phase
B	26.92	14.44	46.31	4.26	7.70	0.37	–	–	–	–	σ phase
C	25.96	27.62	6.94	31.95	5.09	2.71	–	–	–	–	FCC
D	1.91	2.94	0.54	2.28	1.11	–	0.74	3.44	83.32	3.72	Ti (s, s)
E	9.37	14.88	0.44	12.76	–	–	0.59	16.75	42.50	2.71	FCC + Ti (s, s) + Cu(s, s)
F	–	–	–	–	–	–	3.61	93.18	0.30	2.91	Cu(s, s)
G	–	–	–	–	–	–	84.70	10.40	0.55	4.35	Ag (s, s)
H	–	–	–	–	–	–	2.06	66.63	27.93	3.38	Ti–Cu phase

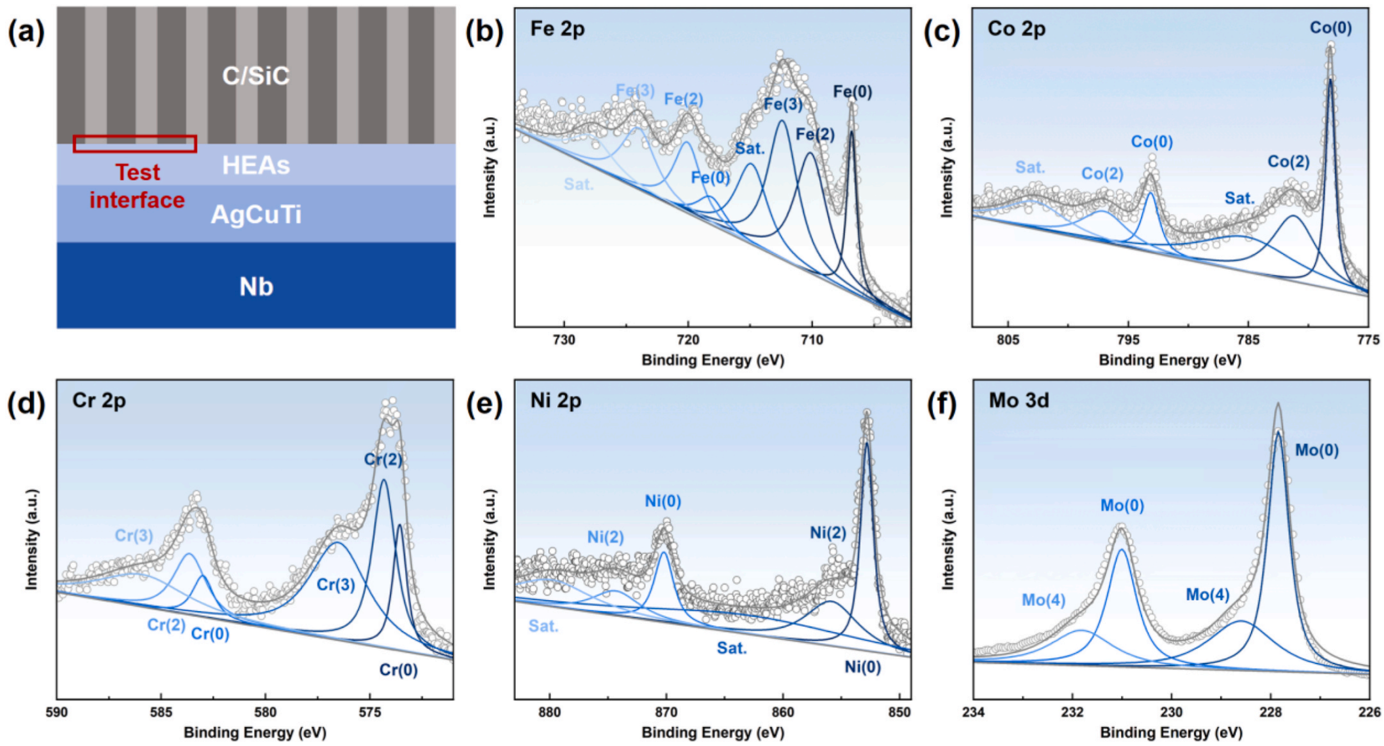

Fig. 6. XPS analysis of the HEML/C/SiC interface
(a) test interface; (b) Fe; (c) Co; (d) Cr; (e) Ni; (f) Mo. (A colour version of this figure can be viewed online.)

phase in both the HEML and C/SiC models. Fig. 7g summarizes these findings, where the adsorption energy of each phase was averaged based on the atomic proportions within the phase. The results show that in the high-entropy alloy phases, the adsorption energy of the BCC phase was slightly lower than that of SiC, while the FCC, σ, and μ phases exhibited higher adsorption energies. This indicates that these phases have a stronger affinity for Ti than the C/SiC substrate. Since the BCC phase constitutes a minor joint of the HEML, the overall adsorption capacity of the HEML is stronger than that of the C/SiC substrate. This finding suggests that the HEML enhances the stability of the AgCuTi filler interaction with the base material, outperforming a direct C/SiC-to-AgCuTi interface. The adsorption energies also reflect the adaptability of the layer in bonding with Ti, particularly in the FCC phase, which shows the highest adsorption energy at 9.3095 eV. This high energy indicates a strong bond, enhancing interfacial strength and improving filler wettability. The BCC and μ phases follow with moderate adsorption energies (6.8721 eV and 4.4222 eV, respectively), contributing with additional stability but allowing a degree of flexibility at the interface. The σ phase and certain sites on the C/SiC substrate show comparatively lower adsorption energies, indicating weaker interactions that may allow stress relief at the interface. Carbon, with an adsorption energy of −0.8112 eV, shows limited affinity for Ti, suggesting that Ti preferentially bonds to SiC rather than pure carbon. In summary, the DFT analysis in Fig. 7 confirms that the HEML, with its varied phase composition and high adsorption energies, forms a stable and robust interface with the AgCuTi filler alloy. The high-entropy alloy's capacity to hold Ti atoms more effectively than C/SiC enhances interfacial wettability, supports strong bonding, and reduces the likelihood of interfacial gaps or weaknesses.

The above research demonstrated that C/SiC and Nb brazed joints joined with AgCuTi filler alloy achieve an ideal microstructure and strong interfacial stability following UHNF-induced high-entropy metallization, supporting the feasibility of our design approach. To determine the optimal thickness of the HEML, we brazed C/SiC with non-HEML, 50 μm, 170 μm, and 350 μm HEML layers to Nb joints using the same filler alloy at 880 °C for 10 min. The resulting microstructures of these brazed joints are shown in Fig. 8. As seen in Fig. 8a, the interface between AgCuTi and C/SiC without an HEML layer displayed a discontinuous metallic compound brittle phase. Studies [12] suggest that this diffusion reaction layer consists mainly of TiC and Ti_5Si_3. The presence of this brittle phase prevents the reaction layer from absorbing stress through plastic deformation, especially under high load or high residual stress conditions. This vulnerability leads to crack formation, with cracks propagating along the interface of the reaction layer, severely limiting the mechanical properties of the brazed joints. Additionally, due to the significant coefficient of thermal expansion (CTE) mismatch between AgCuTi ($17 \times 10^{-6}\ K^{-1}$) and C/SiC ($2.8 \times 10^{-6}\ K^{-1}$), substantial residual stress is introduced in the joint. In high-temperature environments, this stress concentration, coupled with reduced material toughness, increases the likelihood of crack formation, ultimately leading to joint failure and preventing the filler alloy from achieving its maximum operating temperature. Moreover, the filler alloy layer in the brazed joint without HEML was only about 30 μm thick, indicating severe filler alloy flooding. This limited thickness suggests poor interaction between the AgCuTi filler alloy and the C/SiC interface, consistent with the calculated adsorption energies in Fig. 7. In the sample with a 50 μm HEML layer, the microstructure of the brazed joints showed improvement, as depicted in Fig. 8b. The filler alloy flooding was reduced, with the filler alloy region widening to around 60 μm, suggesting that the HEML layer alleviates flooding to some extent. However, due to the thin HEML, the improvement was minimal, and defects persisted at certain points along the HEML-AgCuTi interface. When the HEML thickness increased to 170 μm, the filler alloy flooding issue was substantially reduced, and the interaction at the HEML-AgCuTi interface improved significantly, as shown in Fig. 8c. This thickness appears to offer an effective balance, reducing defects and enhancing the overall stability of the interface. At a 350 μm HEML thickness, as depicted in Fig. 8d, flooding was further mitigated, but more defects appeared in localized regions of the HEML. These defects are likely influenced by the brazing process parameters, which may affect uniformity in thicker

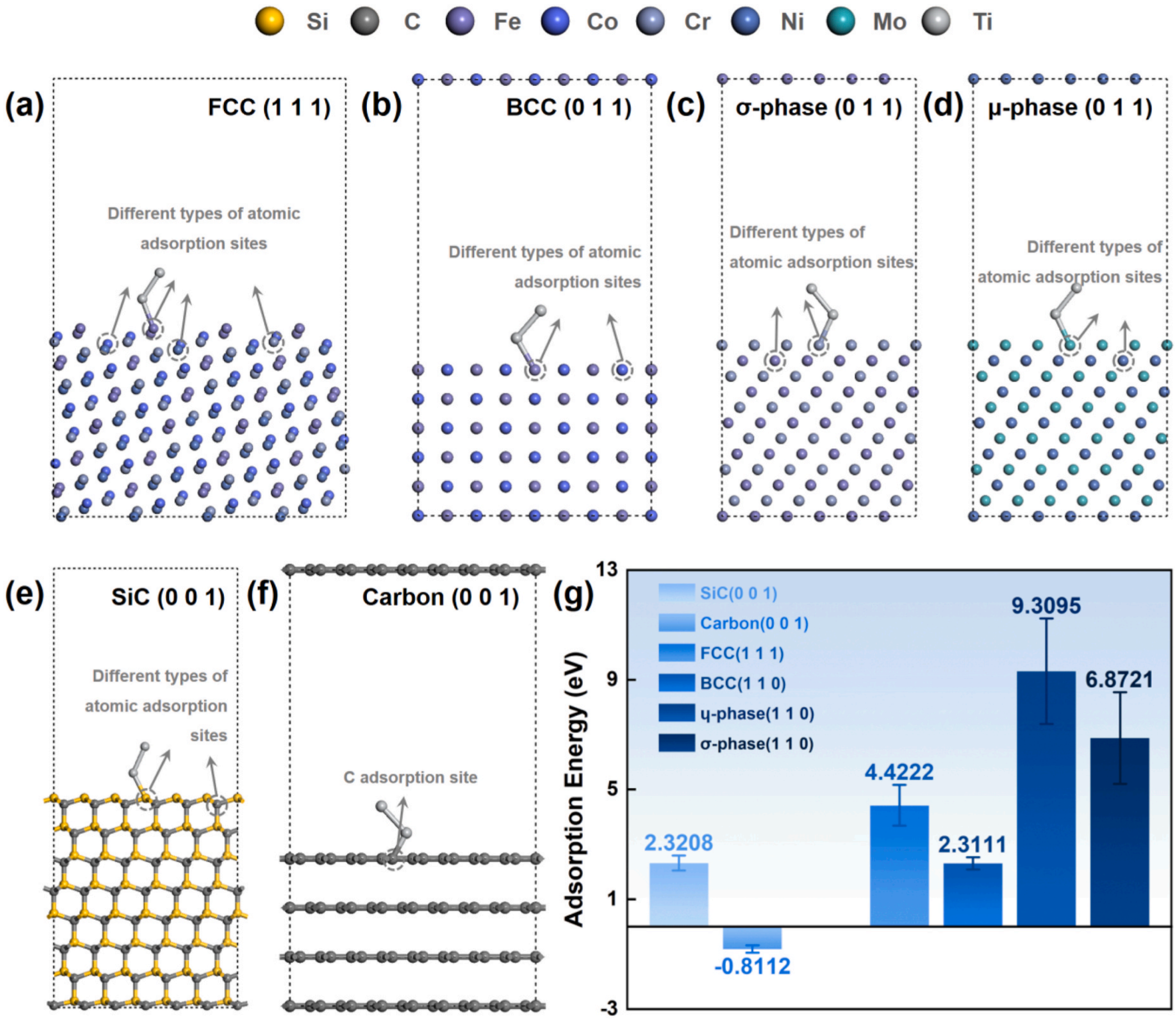

Fig. 7. The adsorption activity of different phases to Ti atoms
(a) FCC; (b) BCC; (c) σ phase; (d) μ phase; (e) SiC; (f) Carbon (g) Adsorption Energy of different phase. (A colour version of this figure can be viewed online.)

HEML layers. In summary, the 170 μm HEML appears to offer the optimal balance between mitigating filler alloy flooding and minimizing interfacial defects, providing a stable interface that enhances mechanical properties and resistance to thermal stress in C/SiC–Nb heterogeneous joints.

To investigate the impact of different HEML thicknesses on relieving residual stress in brazed joints, we conducted a stress analysis, with results displayed in Fig. 9. Fig. 9a–d illustrates the stress distribution for joints without an HEML, and with 50 μm, 170 μm, and 350 μm HEML layers, respectively. The residual stress was measured along the path indicated in each figure, and the results are summarized in Fig. 9e. The data revealed that, without an HEML, stress concentration is severe, primarily localized at the interface between the C/SiC and the AgCuTi filler alloy. This stress concentration significantly limits the temperature range that the filler alloy can withstand. As the HEML thickness increases, the stress concentration at the C/SiC–AgCuTi interface is gradually reduced, with stress progressively transferring into the HEML itself. For the 50 μm HEML layer, a distributed point of stress concentration remains at the HEML-AgCuTi interface, indicating that the thinner layer has limited capacity for stress relief. This also corresponds to the interfacial defects observed in Fig. 8b, where the thin HEML could not fully relieve stress. At an HEML thickness of 170 μm, stress concentration is further alleviated, shifting into the HEML layer. The abundant lattice distortions within the HEML allow for local plastic deformation and a stress relaxation mechanism, effectively dispersing thermal stress and reducing concentration at critical points. However, When the HEML thickness is increased to 350 μm, the stress relief effect remained similar to that at 170 μm, suggesting that 170 μm is the optimal thickness for maximizing stress relief in the HEML. These findings indicate that the stress-relieving capability of the HEML reaches an optimal limit at c. a. ~170 μm. Beyond this thickness, additional material does not significantly enhance stress distribution, suggesting that this thickness is near ideal for balancing stress relief and material efficiency in heterogeneous joints.

To evaluate the effect of HEML thickness on the mechanical properties of the brazed joints, shear tests were conducted on samples with different HEML thicknesses. The results are shown in Fig. 10a. Without an HEML, the shear strength of the room-temperature (RT) brazed joint was 77 MPa. When an HEML was added, the shear strength initially increased with HEML thickness, peaking at 170 μm, and then slightly decreased. At 170 μm, the maximum average shear strength reached 177 MPa, which is 2.3 times greater than the joint without HEML. This improvement indicates that a 170 μm HEML effectively relieves residual stress in C/SiC and Nb brazed heterogeneous joints. The analysis suggests that with a thinner HEML, residual stress is concentrated in the HEML layer, which has limited load-bearing capacity. This results in interfacial defects at the HEML/AgCuTi interface, reducing the joint's overall strength. As the HEML thickness increases, the interfacial load-bearing capacity and shear strength improve. At 170 μm, the HEML optimally balances stress relief and mechanical strength. However,

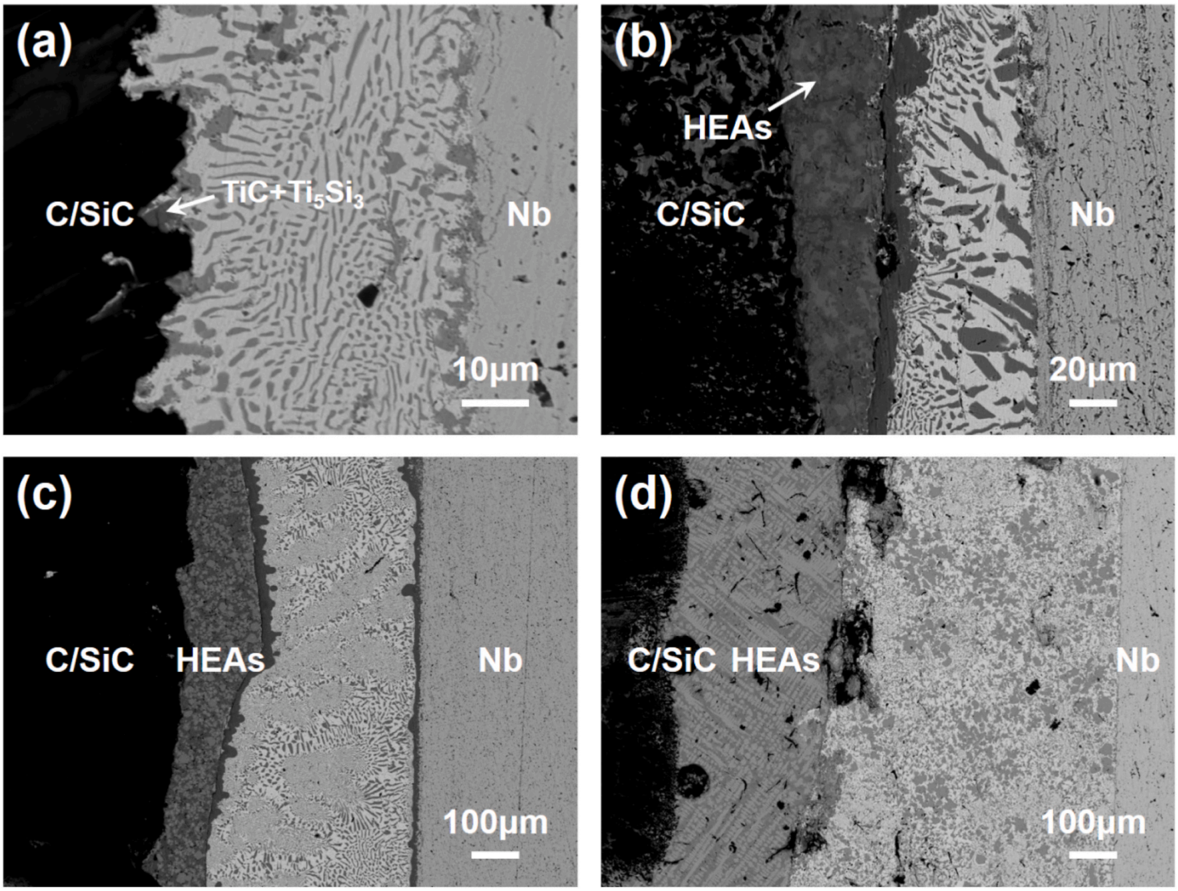

Fig. 8. Microstructure of HEML C/SiC and Nb brazed joints with different thicknesses
(a) 0 μm; (b) 50 μm; (c) 170 μm; (d) 350 μm. (A colour version of this figure can be viewed online.)

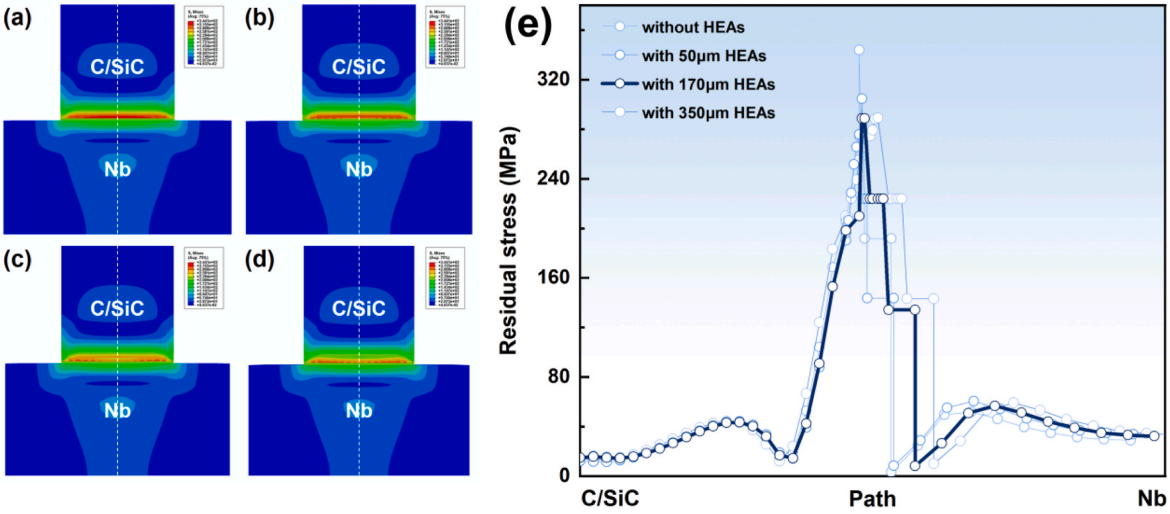

Fig. 9. Stress distribution of C/SiC and Nb brazed joints with different thicknesses HEML
(a) 0 μm; (b) 50 μm; (c) 170 μm; (d) 350 μm; (e) Path residual stress. (A colour version of this figure can be viewed online.)

when the HEML thickness exceeds 170 μm, the presence of minor defects in the thicker HEML slightly reduces the mechanical properties of the joint. Further high-temperature shear tests were conducted at RT and 500 °C to assess the impact of the HEML on performance under elevated temperatures, with results shown in Fig. 10b. At 500 °C, the average shear strength of the brazed joint was 102 MPa, demonstrating excellent performance. This confirms that with the current design strategy, the use of AgCuTi filler alloy in brazed joints maintains reliable mechanical properties at 500 °C, effectively enhancing the high-temperature performance of the filler alloy. To further analyze fracture behavior, stress-strain curves were examined, as shown in Fig. 10c. Without an HEML, the brazed joint exhibited sudden failure, fracturing abruptly at a strain of about 7 %. However, with a 170 μm HEML, the joint began to fracture at a strain of 32 %, nearly three times the strain of the non-HEML

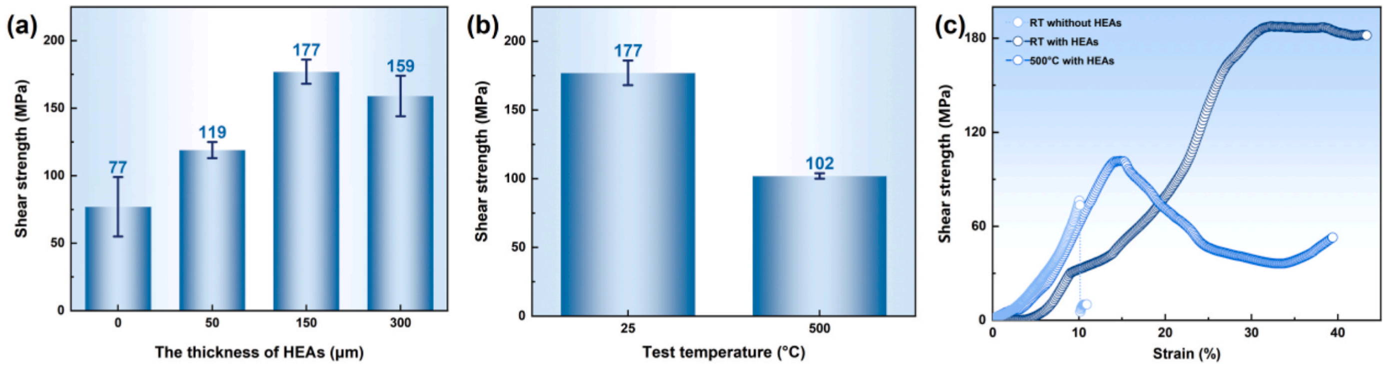

Fig. 10. Mechanical properties of HEML C/SiC and Nb brazed joints
(a) Shear strength of different thickness HEML C/SiC and Nb brazed joints; (b) Shear strength of HEML C/SiC and Nb brazed joints at RT and 500 °C; (c) Stress-strain curves. (A colour version of this figure can be viewed online.)

sample. A plateau appeared in the stress-strain curve, indicating that the HEML altered the fracture path, enhancing resistance to plastic deformation and significantly improving the mechanical properties. At 500 °C, fracture occurred at a strain of approximately 15 %, but the joint did not completely lose its load-bearing capacity; instead, it gradually declined, indicating a more controlled failure. These results show that the HEML effectively optimizes the mechanical performance of brazed joints at both room and high temperatures, allowing AgCuTi filler alloy to perform reliably up to 500 °C.

To examine the effect of HEML on the fracture path and mechanism of brazed joints, we analyzed the fracture microstructure under various conditions. Fig. 11a–b show the fracture microstructure without HEML at room temperature (RT), Figs. 11c–d display the microstructure with HEML at RT, and Figs. 11e–f illustrate the microstructure with HEML at 500 °C. Across all conditions, fractures primarily occurred at the C/SiC interface. Without HEML, the fracture path is relatively flat, indicating a brittle fracture mode, as supported by the stress-strain curve in Fig. 10c. This brittle fracture mode results in low strain capacity and rapid failure. In contrast, when HEML is present, the fracture surface of the C/SiC composite shows evident fiber breakage and pull-out, with a more difficult fracture path. This indicates a shift to a ductile fracture mode, suggesting that the HEML enhances deformation resistance in the brazed joint. The retention of high-entropy alloy (HEA) residues on the fracture surface further confirms that the HEML effectively alleviates residual stress, allowing for greater plastic deformation and improving overall toughness. At 500 °C, the fracture remains concentrated at the C/SiC interface, while the interface between the AgCuTi filler alloy and HEML remains intact, showing that this region is not a weak link in the joint. This observation demonstrates that the AgCuTi filler alloy maintains reliable performance even at elevated temperatures. The ductile fracture mode observed at 500 °C, along with retained HEA residues on the exposed C/SiC fibers, indicates that the HEML continues to provide effective deformation resistance under high-temperature conditions. In summary, the UHNF high-entropy metallization strategy effectively reduces residual stress during the brazing process, enhances the ductility of the fracture path, and significantly improves the high-temperature performance of AgCuTi filler alloy in brazed joints.

4. Conclusion

This study addresses the challenges of excessive residual stress and limited high-temperature performance in the brazing of C/SiC and Nb brazed joints. We propose a UHNF-based high-entropy surface metallization (HEML) technique to alleviate residual stress and enhance the high-temperature performance of the AgCuTi brazing filler alloy. The main conclusions are as follows.

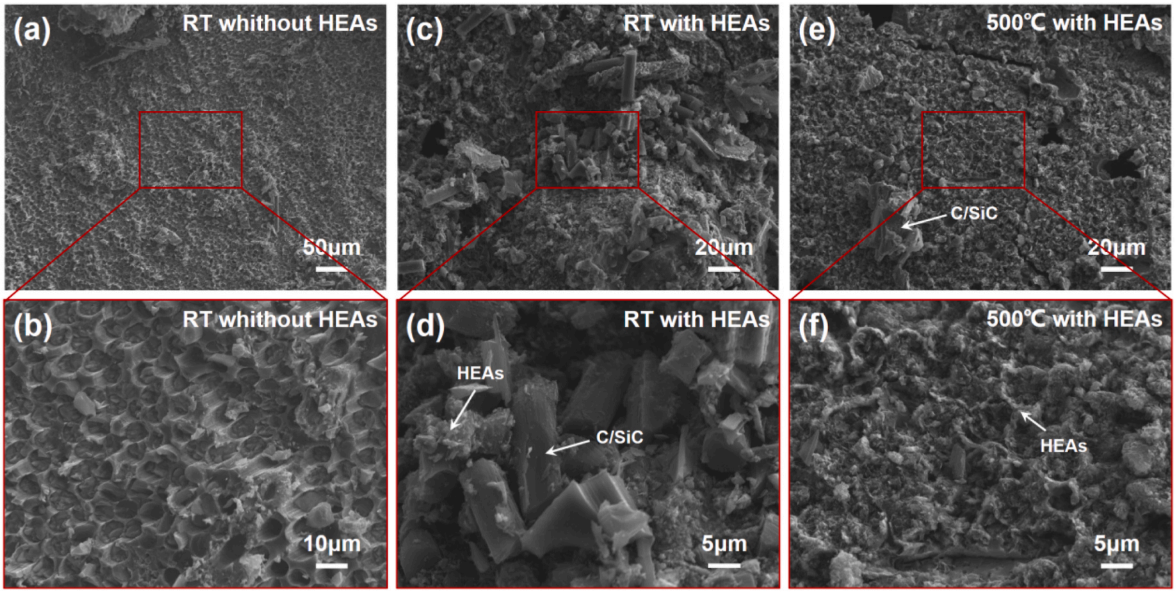

Fig. 11. The fracture microstructure of HEML C/SiC and Nb brazed joints
(a, b) without HEML at RT; (c, d) with HEML at RT; (e, f) with HEML at 500 °C. (A colour version of this figure can be viewed online.)

(1) The UHNF process successfully forms a high-quality HEML on the C/SiC surface through rapid heating and quenching. An increase in current and time causes splashing of HEAs due to rapid cooling results in a thinner HEML. Under optimal conditions (e.g., 50 A for 10 s), a 170 μm thick HEML with a smooth, hole-free surface can be achieved.

(2) The HEML primarily consists of FCC, μ, σ, and BCC phases. The ultra-fast heating accelerates the formation of high-hardness μ and σ phases by minimizing atomic diffusion, while rapid quenching stabilizes these high-temperature phases at room temperature. Significant lattice distortion within the HEML provides enhanced dislocation pathways, improving resistance to plastic deformation in the brazed joint.

(3) The HEML establishes strong bonding at the C/SiC–Nb interface. A thin reaction layer of high-entropy carbides and silicides forms at the HEML/C/SiC interface, mitigating brittleness typically associated with thicker layers. At the HEML-AgCuTi filler alloy interface, Ti accumulation indicates good adhesion. The higher adsorption capacity for Ti of the HEML compared to C/SiC suggests a stronger and more stable interaction with the AgCuTi alloy.

(4) Without an HEML, the AgCuTi/C/SiC interface readily forms discontinuous brittle compounds, causing cracks under high stress and temperature, thus limiting mechanical performance and maximum operating temperature. Increasing the HEML thickness shifts stress concentration from the C/SiC–AgCuTi interface into the HEML, reducing overflow of the AgCuTi alloy. A 170 μm HEML provides optimal stress relief; thicker layers introduce internal defects without further enhancement of stress relief.

(5) The shear strength of the RT brazed joint without HEML is 77 MPa. Adding the HEML initially increases shear strength with thickness, peaking at 177 MPa with a 170 μm HEML (2.3 increase). This demonstrates the effectiveness of the HEML in stress relief and mechanical enhancement. At 500 °C, the 170 μm HEML maintains a shear strength of 102 MPa, highlighting the AgCuTi filler alloy’s improved high-temperature performance.

(6) Without HEML, the joint undergoes brittle fracture at a strain of approximately 7 %, with a straight fracture path and rapid failure. With a 170 μm HEML, fracture occurs at a strain of around 32 %, displaying a more difficult fracture path and enhanced toughness. At 500 °C, the joint fractures at a strain of ∼15 % but fails gradually, with fracture primarily occurring at the C/SiC interface. The HEML-AgCuTi interface remains stable, confirming reliable performance at high temperatures.

In conclusion, the UHNF surface high-entropy metallization strategy effectively reduces residual stress, enhances toughness, and significantly improves the high-temperature reliability of AgCuTi brazing filler alloy in C/SiC–Nb brazed joints.

CRediT authorship contribution statement

Peixin Li: Writing – original draft, Software, Investigation, Formal analysis, Data curation. **Zeyu Wang:** Investigation, Funding acquisition, Data curation. **Yicheng Chen:** Investigation, Formal analysis, Data curation. **Hassaan Ahmad Butt:** Investigation, Data curation. **Zilong Zhang:** Investigation, Data curation. **Ziyao Huang:** Investigation, Data curation. **Tianlei Zhang:** Investigation, Data curation. **Liang Qiao:** Software. **Ying Zhong:** Investigation, Formal analysis, Data curation. **Dmitry Krasnikov:** Investigation, Data curation. **Albert Nasibulin:** Investigation, Data curation. **Jian Cao:** Resources. **Yaotian Yan:** Writing – review & editing, Resources, Funding acquisition, Conceptualization. **Junlei Qi:** Writing – review & editing, Resources, Funding acquisition, Conceptualization.

Declaration of competing interest

The authors declare that they have no known competing financial interests or personal relationships that could have appeared to influence the work reported in this paper.

Acknowledgments

P. Li and Z. Wang contributed equally to this work. This work was supported by the National Natural Science Foundation of China (Grant Nos. 524B200166, Grant Nos. 52175303, Grant Nos. 5240051808), The National Science Fund for Distinguished Young Scholars (Grant Nos. 52125502), Hainan Province Science and Technology Special Fund (Grant No. ZDYF2024SHFZ082), Postdoctoral Fellowship Program of CPSF under Grant Number GZB20240949, State Key Laboratory of Precision Welding & Joining of Materials and Structures (24-R-01; 24-Z-07), the Natural Science Foundation of the Jiangsu Higher Education Institutions (Grant Nos. 23KJB430008), the Natural Science Foundation of Jiangsu Province (Grant Nos. BK20230531). Special thanks to HIT Center of Analysis Measurement and Computing and Dr. Zheng Zhen for the electron microscope test analysis.

References

[1] T. Dursun, C. Soutis, Recent developments in advanced aircraft aluminium alloys, Mater. Des. 56 (2014) 862–871.
[2] Y. Hao, Z. Leng, C. Yu, P. Xie, L. Zhou, Y. Li, G. Liang, X. Li, C. Liu, Ultra-lightweight hollow bowl-like carbon as microwave absorber owning broad band and low filler loading, Carbon 212 (2023) 118156.
[3] Z.-Y. Wei, G.-H. Meng, L. Chen, G.-R. Li, M.-J. Liu, W.-X. Zhang, L.-N. Zhao, Q. Zhang, X.-D. Zhang, C.-L. Wan, Z.-X. Qu, L. Chen, J. Feng, L. Liu, H. Dong, Z.-B. Bao, X.-F. Zhao, X.-F. Zhang, L. Guo, L. Wang, B. Cheng, W.-W. Zhang, P.-Y. Xu, G.-J. Yang, H.-N. Cai, H. Cui, Y. Wang, F.-X. Ye, Z. Ma, W. Pan, M. Liu, K.-S. Zhou, C.-J. Li, Progress in ceramic materials and structure design toward advanced thermal barrier coatings, J. Adv. Ceram. 11 (2022) 985–1068.
[4] C. Song, F. Ye, L. Cheng, Y. Liu, Q. Zhang, Long-term ceramic matrix composite for aeroengine, J. Adv. Ceram. 11 (2022) 1343–1374.
[5] X. Hernandez, C. Jimenez, K. Mergia, P. Yialouris, S. Messoloras, V. Liedtke, C. Wilhelmi, J. Barcena, An innovative joint structure for brazing C_f/SiC composite to titanium alloy, J. Mater. Eng. Perform. 23 (2014) 3069–3076.
[6] H. Mei, L. Cheng, L. Zhang, Y. Xu, Effect of fiber architectures on thermal cycling damage of C/SiC composites in oxidizing atmosphere, Mater. Sci. Eng. A Struct. Mater. Prop. Microstruct. Process. 460 (2007) 306–313.
[7] D. Zhao, T. Guo, X. Fan, C. Chen, Y. Ma, Effect of pyrolytic carbon interphase on mechanical properties of mini T800-C/SiC composites, J. Adv. Ceram. 10 (2021) 219–226.
[8] L. Yang, X. Xiao, L. Liu, J. Luo, K. Jiang, X. Han, C. Zhao, J. Zhang, G. Wang, Dynamic oxidation mechanism of carbon fiber reinforced SiC matrix composite in high-enthalpy and high-speed plasmas, J. Adv. Ceram. 11 (2022) 365–377.
[9] C. Zhao, Z. Tu, J. Mao, The dynamic thermophysical properties evolution and multi-scale heat transport mechanisms of 2.5D C/SiC composite under high-temperature air oxidation environment, Compos. B Eng. 263 (2023) 110831.
[10] L. Wang, Z. Wang, S.M. Dong, W. Zhang, Y. Wang, Finite element simulation of stress distribution and development of C_f/SiC ceramic-matrix composite coated with single layer SiC coating during thermal shock, Compos. B Eng. 51 (2013) 204–214.
[11] G. Liu, X. Zhang, J. Yang, G. Qiao, Recent advances in joining of SiC-based materials (monolithic SiC and SiC_f/SiC composites): joining processes, joint strength, and interfacial behavior, J. Adv. Ceram. 8 (2019) 19–38.
[12] J. Ba, X. Ji, H. Li, J. Lin, J. Qi, J. Cao, Nano tungsten reinforced carbon cloth interlayer for brazing C/SiC composites to Nb, J. Manuf. Process. 58 (2020) 1270–1273.
[13] X. Tian, J. Feng, J. Shi, Y. Liu, L. Zhang, Interfacial microstructure and mechanical properties of the vacuum brazed C/SiC composite and Nb joints, Vacuum 146 (2017) 97–105.
[14] B. Blakey-Milner, P. Gradl, G. Snedden, M. Brooks, J. Pitot, E. Lopez, M. Leary, F. Berto, A. du Plessis, Metal additive manufacturing in aerospace: a review, Mater. Des. 209 (2021) 110008.
[15] Y. Yan, P. Li, Z. Zhang, Y. Wang, J. Zhang, L. Qiao, J. Cao, J. Qi, Interfacial Si-O coordination for inhibiting the graphite phase enables superior SiC/Nb heterostructure joining by AuNi, Compos. B Eng. 282 (2024) 111557.
[16] Y. Li, L. Wang, Y. Li, H. Wu, B. Tu, G. Liu, M. Lei, Wetting and spreading of bulk liquid and precursor film of molten AgCuTi on ultrafast laser structured surface of Ti, J. Mater. Res. Technol. 29 (2024) 5484–5494.
[17] P. Wang, W. Liu, J. Li, W. Shi, Z. Liu, S. Zhao, X. Nai, H. Chen, Q. Wang, W. Li, Unrevealing the wetting behavior and mechanism of AgCuTi filler on negative thermal expansion $Sc_2W_3O_{12}$ materials: experiments and first-principles calculations, Appl. Surf. Sci. 652 (2024) 159257.

[18] Z.R. Li, Z.Z. Wang, G.D. Wu, J.C. Feng, Microstructure and mechanical properties of ZrB_2-SiC ultrahigh temperature ceramic composite joint using TiZrNiCu filler metal, Sci. Technol. Weld. Join. 16 (2011) 697–701.

[19] M.C. Halbig, B.P. Coddington, R. Asthana, M. Singh, Characterization of silicon carbide joints fabricated using SiC particulate-reinforced ag-cu-ti alloys, Ceram. Int. 39 (2013) 4151–4162.

[20] X. Chen, G. Cheng, J. Zhang, F. Guo, H. Zhou, C. Liao, H. Wang, X. Zhang, S. Dong, Residual stress variation in SiC_f/SiC composite during heat treatment and its effects on mechanical behavior, J. Adv. Ceram. 9 (2020) 567–575.

[21] R. Asthana, M. Singh, Joining of partially sintered alumina to alumina, titanium, hastealloy and C-SiC composite using Ag-Cu brazes, J. Eur. Ceram. Soc. 28 (2008) 617–631.

[22] J. Ba, X.H. Zheng, R. Ning, J.H. Lin, J.L. Qi, J. Cao, W. Cai, J.C. Feng, C/SiC composite-Ti6Al4V joints brazed with negative thermal expansion ZrP_2WO_{12} nanoparticle reinforced AgCu alloy, J. Eur. Ceram. Soc. 39 (2019) 755–761.

[23] B. Zhang, L. Zhang, Z. Sun, Q. Chang, J. Feng, Enhancement of high-temperature oxidation resistance of the AgCu-based alloy by in-situ fabricating three-dimensional TiC nanosheet reinforcement, Corros. Sci. 198 (2022) 110094.

[24] P. Li, Y. Yan, J. Ba, P. Wang, H. Wang, X. Wang, J. Lin, J. Cao, J. Qi, The regulation strategy for releasing residual stress in ceramic-metal brazed joints, J. Manuf. Process. 85 (2023) 935–947.

[25] D. Ni, Y. Cheng, J. Zhang, J.-X. Liu, J. Zou, B. Chen, H. Wu, H. Li, S. Dong, J. Han, X. Zhang, Q. Fu, G.-J. Zhang, Advances in ultra-high temperature ceramics, composites, and coatings, J. Adv. Ceram. 11 (2022) 1–56.

[26] W. Fu, S.P. Hu, X.G. Song, C. Jin, J.X. Li, Y.X. Zhao, J. Cao, G.D. Wang, Effect of Ti content on the metallization layer and copper/alumina brazed joint, Ceram. Int. 43 (2017) 13206–13213.

[27] A.O. Moghaddam, N.A. Shaburova, M.N. Samodurova, A. Abdollahzadeh, E. A. Trofimov, Additive manufacturing of high entropy alloys: a practical review, J. Mater. Sci. Technol. 77 (2021) 131–162.

[28] P. Li, J. Zhang, T. Yang, T. Zhang, J. Zhang, J. Lin, Y. Yan, C. Li, X. Si, J. Cao, J. Qi, Characteristics, applications and perspective of high entropy alloys for interfacial joining: a review, J. Manuf. Process. 110 (2024) 303–317.

[29] Y. Zheng, M. Zou, W. Zhang, D. Yi, J. Lan, C.-W. Nan, Y.-H. Lin, Electrical and thermal transport behaviours of high-entropy perovskite thermoelectric oxides, J. Adv. Ceram. 10 (2021) 377–384.

[30] Y. Tang, R. Wang, B. Xiao, Z. Zhang, S. Li, J. Qiao, S. Bai, Y. Zhang, P.K. Liaw, A review on the dynamic-mechanical behaviors of high-entropy alloys, Prog. Mater. Sci. 135 (2023) 101090.

[31] C. Wang, W. Ping, Q. Bai, H. Cui, R. Hensleigh, R. Wang, A.H. Brozena, Z. Xu, J. Dai, Y. Pei, C. Zheng, G. Pastel, J. Gao, X. Wang, H. Wang, J.-C. Zhao, B. Yang, X. Zheng, J. Luo, Y. Mo, B. Dunn, L. Hu, A general method to synthesize and sinter bulk ceramics in seconds, SCIENCE 368 (2020) 521–526.

[32] C. Dai, T. Zhao, C. Du, Z. Liu, D. Zhang, Effect of molybdenum content on the microstructure and corrosion behavior of $FeCoCrNiMo_x$ high-entropy alloys, J. Mater. Sci. Technol. 46 (2020) 64–73.

[33] S. Lei, Z. Xue, Y. Liu, Y. Li, D. Jiang, P. Wang, Effect of annealing temperature on the structure and properties of FeCoCrNiMo high-entropy alloy, High Temp. Mater. Process. 41 (2022) 417–423.

[34] G.W. Liu, M.L. Muolo, F. Valenza, A. Passerone, Survey on wetting of SiC by molten metals, Ceram. Int. 36 (2010) 1177–1188.

[35] H. Xiang, Y. Xing, F.-z. Dai, H. Wang, L. Su, L. Miao, G. Zhang, Y. Wang, X. Qi, L. Yao, H. Wang, B. Zhao, J. Li, Y. Zhou, High-entropy ceramics: present status, challenges, and a look forward, J. Adv. Ceram. 10 (2021) 385–441.

[36] Y. Qin, J.-X. Liu, F. Li, X. Wei, H. Wu, G.-J. Zhang, A high entropy silicide by reactive spark plasma sintering, J. Adv. Ceram. 8 (2019) 148–152.

[37] M. Liu, H. Wu, Y. Wang, J. Ren, D.A. Alshammari, H.E.A. Elsalam, I.H.E. Azab, H. Algadi, P. Xie, Y. Liu, Flexible cementite/ferroferric oxide/silicon dioxide/carbon nanofibers composite membrane with low-frequency dispersion weakly negative permittivity, Adv. Compos. Hybrid Mater. 6 (2023) 217.

[38] P. Xie, Y. Liu, M. Feng, M. Niu, C. Liu, N. Wu, K. Sui, R.R. Patil, D. Pan, Z. Guo, R. Fan, Hierarchically porous Co/C nanocomposites for ultralight high-performance microwave absorption, Adv. Compos. Hybrid Mater. 4 (2021) 173–185.